ACS Catalysis

pubs.acs.org/acscatalysis Research Article

Effect of Alkali Metal Cations on Nitrate Electroreduction Kinetics, Mass Transport, and Cobalt Catalyst Oxidation

Rajkumar Jana, O. Quinn Carvalho, Ruth Bello, Payal Chaudhary, Jiyun Hong, Adam S. Hoffman, Simon R. Bare, Ankur Gupta, Vitaly Alexandrov, and Kelsey A. Stoerzinger*

Cite This: https://doi.org/10.1021/acscatal.6c02764 Read Online

ACCESS | Metrics & More | Article Recommendations | Supporting Information

ABSTRACT: The electroreduction of the nitrate anion is surprisingly catalyzed on surfaces that are perceived as negatively charged, conditions where cations from the electrolyte are—on average—closer to the surface in the electrical double layer (EDL). As such, the charge density of alkali metal cations and the extent of their interactions with nitrate could notably impact both transport of nitrate to the surface and the rates of its reduction. We separate these effects quantitatively for the electrocatalytic nitrate reduction reaction (NO3RR) on cobalt in alkaline media, which has a high Faradaic efficiency to ammonia (~90%). A K^+-containing electrolyte has higher NO3RR kinetic currents than a Li^+-containing one, though the magnitude of this difference depends on catalyst pretreatment. Surprisingly, an ~2x difference in the apparent NO3RR diffusion limited current is observed between Li^+ and K^+ electrolytes, inconsistent with the reduction of uncharged reactants. This difference arises in part from the availability of active sites, also involved in (oxy)hydroxide formation due to the highly oxidizing nature of the nitrate reactant and nitrite intermediate. The dynamic role of such species during NO3RR is uniquely influenced by the nature of the cation, pointing to a complex coexistence of (hydr)oxides and cations in stabilizing the anionic reactant under the reducing conditions of NO3RR.

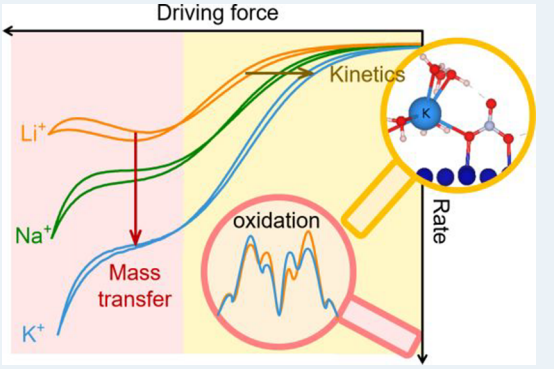

KEYWORDS: *electrochemical nitrate reduction, specific ion effects, electrical double layer, electrolyte effects, X-ray absorption spectroscopy, metal redox, open circuit potential*

1. INTRODUCTION

At potentials where electrocatalysts are negatively charged, electrostatics indicates cations are closest to the surface,[1] dominating the Stern layer with a thickness comparable to that of a solvated ion.[2] As such, the nature of the cation in solution has been observed to impact the rate of electroreduction reactions such as the oxygen reduction reaction (ORR),[3] carbon dioxide reduction reaction (CO2RR),[4−7] and hydrogen evolution reaction (HER).[8−11] The origin of such effects can be complex and vary across catalysts and reactions. For example, changes in the electric field strength impact electron transfer for rate-determining intermediates[12,13] with large dipole moments, and reduction reactions in alkaline electrolytes uniquely require abstracting protons from water, where dissociation constants can be influenced by cation identity.[14,15]

For nitrate electroreduction (NO3RR), the anticipated effect of cation identity is more complex due to the negative charge of the reactant.[16] Surprisingly, NO3RR occurs at high rates[17] on many metals below the potential of zero total charge (PZTC),[18] under conditions where transport of anions to the surface is unfavorable,[19−21] with counter cations instead anticipated to be closest to the electrode surface. Thus, in addition to cation effects at length scales of the Stern layer (Ångströms) described above,[1,4,5,22,23] ion pairing may influence transport to the near-surface region (micrometers), particularly under high nitrate concentrations where migration may significantly act against diffusive transport.[24,25] Initial investigations indeed demonstrate the identity of cation matters;[26−28] however, these investigations convolve kinetics with the impact of mass transport and changes in the local reaction environment,[29] and are on catalysts yielding multiple products, where series reactions hinder kinetic quantification.[30] Against this backdrop is further complexity that NO_3^- is highly oxidizing and may lead to oxide formation upon dissociative adsorption on some metals, such as cobalt and copper,[17,31−34] (dependent upon the electrochemical potential and pH).

Received: April 9, 2026
Revised: June 29, 2026
Accepted: July 8, 2026

Here, we quantify the effect of cation identity for the NO3RR on cobalt (Co), where our previous work has shown Co to be uniquely capable amongst first row transition metals in achieving high Faradaic efficiency (FE) to ammonium in bulk neutral media.[35] Cobalt has subsequently attracted much attention for NO3RR in alkaline environments as well, where this selectivity is maintained.[36,37] Here, we employ forced convection electrochemical techniques using a rotating disk electrode (RDE) geometry to quantify diffusion-limited rates, surprisingly ~2x higher in K^+ than Li^+, and account for these differences in rigorous quantification of kinetic current. The NO3RR kinetic currents are ~2–3x higher in K^+- than Li^+-containing electrolytes, where density functional theory (DFT) calculations support the stabilization of nitrate adsorption via the inclusion of a cation, and to a greater extent with K^+. A stronger electric field strength for K^+ resultant from its smaller hydrated radius than Li^+ is also consistent with these greater rates in K^+-containing electrolytes, given the polar intermediates involved in the initial reduction of NO_3^- to NO_2^-. Differences in mass transfer-limited rates with cation identity are an order of magnitude larger than for the inner sphere reduction of uncharged reactant species (e.g., O_2)[3] or outer-sphere electron transfer to anions (e.g., $[Fe(CN)_6]^{3-}$),[38] which, together with operando X-ray absorption spectroscopy (XAS) measurement, suggest the dynamic formation of (hydr)oxides during NO3RR varies with cation identity.

2. METHODS

2.1. Electrochemistry

Semiconductor-grade metal hydroxide pellets, trace metal grade nitrate salts (see Supporting Information for vendors), and Milli-Q water (18.2 MΩ·cm, <10 ppb TOC, Milli-Q IQ 7010) were used for the preparation of all the aqueous electrolytes. Prior to each electrochemical experiment, the electrolyte was saturated with ultrahigh-purity argon gas.

For RDE, a cobalt disk (Pine research, 99.95%) was used as a working electrode with a high-purity Pt coil counter electrode and a Ag/AgCl (CH Instruments, CHI 111, saturated KCl) reference electrode in an undivided PFA electrochemical cell with a custom-machined polytetrafluoroethylene (PTFE) cap. The reference electrode was experimentally calibrated to the reversible hydrogen electrode (RHE) before each experiment in the relevant 0.138 M *M*OH electrolyte and isolated with a secondary frit (Ametek K0065) during measurements. Cyclic voltammetry (CV) and linear sweep voltammetry (LSV) measurements were performed at 10 and 2 mV/s scan rates, respectively. All reported potentials have been corrected for the measured uncompensated resistance (typically, 35–45 Ω) from potentio electrochemical impedance spectroscopy (PEIS) at the open circuit potential. The current has been normalized by the geometric surface area of the cobalt disk (0.19625 cm^2).

Before activity measurements, two separate methods were adopted for cleaning the cobalt disk. 1) HCl etching of residual oxides, performed by etching with 1:4 HCl:H_2O for 30 s, followed by thoroughly rinsing with Milli-Q water and drying under nitrogen flow, referred to as "HCl pretreatment" in the text. 2) An electrochemical method, referred to as "OCP pretreatment" in the text. After mechanical polishing, the electrode was held at –0.37 V vs RHE for 30 min in 0.138 M *M*OH to pre-reduce any remaining oxides and *M*NO_3 was added while holding the Co disk at +0.3 V vs RHE (a constant potential similar to OCP in the presence of nitrate) for 3 min and 10 s.

Product selectivity was measured for Co foil (Beantown Chemical, ≥99.5%) in a PTFE H-cell with a Ag/AgCl reference electrode in a secondary frit, separated with Fumasep FAA-3-50 membrane from graphitic carbon rods (Becker Brothers) as a counter electrode. Nitrate and nitrite were quantified by anion ion chromatography (Thermo Scientific Dionex Integrion HPIC system), and NH_3 by a modified Berthelot reaction.[39] More details are provided in the Supporting Information.

2.2. Operando X-ray Absorption Spectroscopy (XAS)

Operando Co K-edge XAS spectra were collected at beamline 9–3 of the Stanford Synchrotron Radiation Lightsource at the SLAC National Accelerator Laboratory. The photon energy was selected using a liquid-nitrogen-cooled, double-crystal Si (220) monochromator (crystal orientation φ=0°). XAS data were collected in fluorescence mode using a passivated implanted planar silicon (PIPS) detector. The I_0 signal was recorded using a N_2-filled ion chamber. For energy calibration, a Co foil standard (7.5 μm thickness) was scanned simultaneously with every scan using an off-axis photodiode.

The operando flow cell was based on cell design by Ostervold et al.[40] The flow rate was 10 ml/min, and the working electrode comprised 20 wt % Co nanoparticles (~25 nm particle size) supported on Vulcan carbon (20 wt % Co on Vulcan XC-72, Premetek) drop cast on a 25 × 25 mm piece of 0.3 mm thick glassy carbon. Co nanoparticles were first reduced to remove residual oxide and achieve a metallic state by holding at –0.56 V vs RHE for 115 min until the spectra did not change appreciably with time and then stepped sequentially to less cathodic potentials. Additional details are provided in the Supporting Information.

2.3. Density Functional Theory (DFT)

All spin-polarized DFT calculations were performed using the Vienna Ab initio Simulation Package (VASP).[41,42] The projector augmented wave (PAW) pseudopotentials (Co, K_sv, Li_sv, N, O, and H) were used,[43] and exchange-correlation functionals were described using the Perdew-Burke-Ernzerhof (PBE) scheme.[44] A plane-wave kinetic energy cutoff of 400 eV was used, and the electronic self-consistency convergence threshold was set to 10^{-4} eV. Nonlocal van der Waals interactions were described using the DFT-D3 method based on Grimme's formalism.[45] The Co(0001) surface was modeled using a four-layer thick metal slab with lateral dimensions of 9.71 Å × 8.41 Å. A vacuum spacing of 21 Å was introduced along the surface-normal direction to prevent interactions between periodic slab images. Structural optimizations were performed by relaxing all adsorbates and the top two layers of the slab until residual forces were below 0.05 eV/Å. The Brillouin zone was sampled using a Monkhorst–Pack k-point mesh of 3 × 3 × 1. DFT binding energies were computed following the methodology described in the literature.[46] For adsorbed species, only vibrational entropy effects were considered, consistent with previous studies.[46] Further details are provided in supporting Information.

3. RESULTS AND DISCUSSION

The NO3RR activity of a polycrystalline Co disk, precleaned of native oxide with dilute HCl prior to measurement, was measured using CV. The rotation rate of an RDE controls the thickness of a diffusive boundary layer, enabling systematic manipulation of mass transfer to the catalyst surface. Figure 1 illustrates that increasing the concentration of KNO_3 in 0.138 M KOH leads to the onset of NO3RR current around –0.1 V vs RHE, the magnitude of which increases with bulk KNO_3 concentration. In the presence of KNO_3, two characteristic regions are observed upon sweeping to more negative potentials: a steep onset characteristic of rates dominated by kinetics (shaded in yellow), followed by an approximately voltage-independent rate dominated by mass transfer limitations (shaded in red). We note the investigation of low KNO_3 concentrations with a >35x larger concentration of supporting electrolyte (0.138 M KOH) mitigating contributions from

https://doi.org/10.1021/acscatal.6c02764
ACS Catal. XXXX, XXX, XXX–XXX

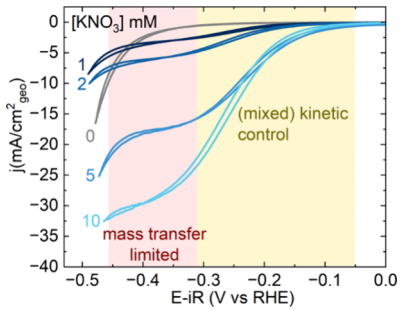

Figure 1. CVs at 10 mV/s from a cobalt disk rotating at 400 rpm, measured in 0.138 M KOH with noted concentration in mM of KNO_3. The region highlighted in yellow shows the steep onset of NO3RR dominated by kinetics, whereas the red region shows the ~voltage-independent current arising from mass transport limitations. The CV with 0 mM KNO_3 illustrates the onset of HER in the absence of NO_3^-.

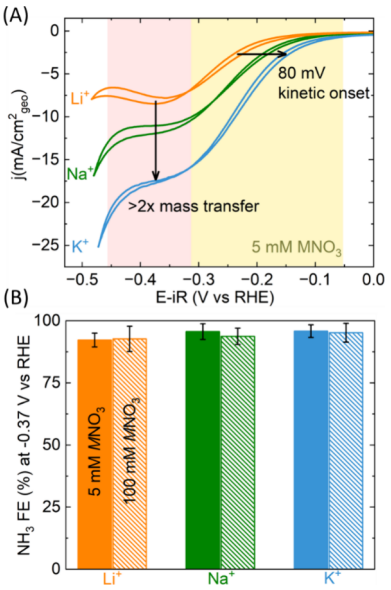

Figure 2. Cobalt NO3RR in 0.138 M *M*OH. A) Variation in current density response with cation identity at 400 rpm with 5 mM MNO_3. Differences in onset are highlighted for –1 mA/cm^2. B) Average NH_3 FE at –0.37 V vs RHE in noted concentration of MNO_3; error bars represent the standard deviation of three independent measurements.

migration, such that mass transfer is dominated by diffusion in the stagnant layer (see Supporting information).

Surprisingly, both regions of the CV show notable changes with cation identity, suggesting that kinetic rates *and* mass transfer improve in the order $Li^+ < Na^+ < K^+$ (Figure 2a). We note that this difference in current does not arise from changes to the FE or number of electrons transferred in NO3RR; NH_3 FE remains ~90% regardless of cation identity or MNO_3 concentration (Figure 2b). The differences in diffusion limited current are in contrast to that for the oxygen reduction reaction (ORR), where ORR has comparable diffusion limited rates for Co in 0.138 M LiOH and KOH (Figure S1), in agreement with the literature on other catalysts.[3] We also observe cation effects on NO3RR rates in neutral buffered solution, illustrating that the presence of other anions does not mitigate these effects (Figure S2).

3.1. Separating Kinetic- and Mass Transfer-Limited Rates

We first consider the impact of cation identity on the kinetic current. The difference in observed onset potentials with cation identity is supportive of kinetic effects (Figure 2a), with ~80 mV shifts, nearly twice that observed in the ORR on other metals.[3] The rotation rate dependence of the current (Figures 3a and S3) can be leveraged to isolate and quantify kinetic currents (from diffusion-limited ones, which we discuss differ with cation in Section 3.3) by extrapolating to infinite rotation rates using the Koutecky–Levich equation:[47]

$$1/j = (1/j_k) + (1/j_d) \quad (1)$$

where j is the measured current density, whose inverse can be considered as the sum of the inverse of kinetic and diffusion limited current densities, j_k and j_d , respectively. The diffusion-limited current density is linearly dependent on the square root of the angular rotation rate of the RDE, ω:

$$j_d = (0.62nFD_{eff}^{2/3}\nu^{-1/6}C^*) \times \omega^{1/2} \quad (2)$$

where n is the number of electrons transferred, F is Faraday's constant, D_{eff} is the effective diffusion coefficient of reactant, ν is the kinematic viscosity, and C^* is the concentration in the bulk electrolyte. Thus, the Koutecky–Levich (K–L) analysis gives a straight line plotting $1/j$ vs $\omega^{-1/2}$ with a K–L slope (eq 3), which we indeed observe here (Figures 3b and S4). The effective diffusion coefficient values calculated using eq 3 are tabulated in Table S2.

$$\text{K} - \text{L slope} = 1/(0.62nFD_{eff}^{2/3}\nu^{-1/6}C^*) \quad (3)$$

3.2. Kinetic Rates

We isolate the effect of cations on the kinetic current in alkaline media via Koutecky–Levich analysis, finding NO3RR rates that are 2–3x higher in K^+-containing electrolyte compared to those containing Li^+ (Figures 3c and S5). Comparable rate differences with cation are observed for measurements on an electrochemically reduced surface as well (Figure S6). Considering the ~90% FE toward NH_3 enables calculation of kinetic rates of NH_3 production: 120 ± 3, 172 ± 5, and 278 ± 7 μmol cm_{geo}^{-2} h^{-1} for Li^+, Na^+, and K^+, respectively, for the polycrystalline cobalt disk in 5 mM MNO_3-containing media at –0.3 V vs RHE. Moreover, the observed NO3RR rate is approximately first order with respect to nitrate concentration (Figure S7). These rates represent the first, known to us, that account for cation-dependent mass transfer limitations in NO3RR.

We next consider the role of cations in influencing both the interfacial electric field and intermediate adsorption energies. The smaller hydrated radius of K^+ leads to closer approach to the Co surface (Figure 4). Accounting for cation-dependent potential drops within the Stern layer is consistent with the experimentally observed differences in NO3RR kinetic rates (Figure S8). We note a similarly ~2x greater HER current density for K^+ vs. Li^+ electrolytes in the absence of MNO_3 (Figure S9). The closer approach of K^+ and its weaker solvation

https://doi.org/10.1021/acscatal.6c02764
ACS Catal. XXXX, XXX, XXX–XXX

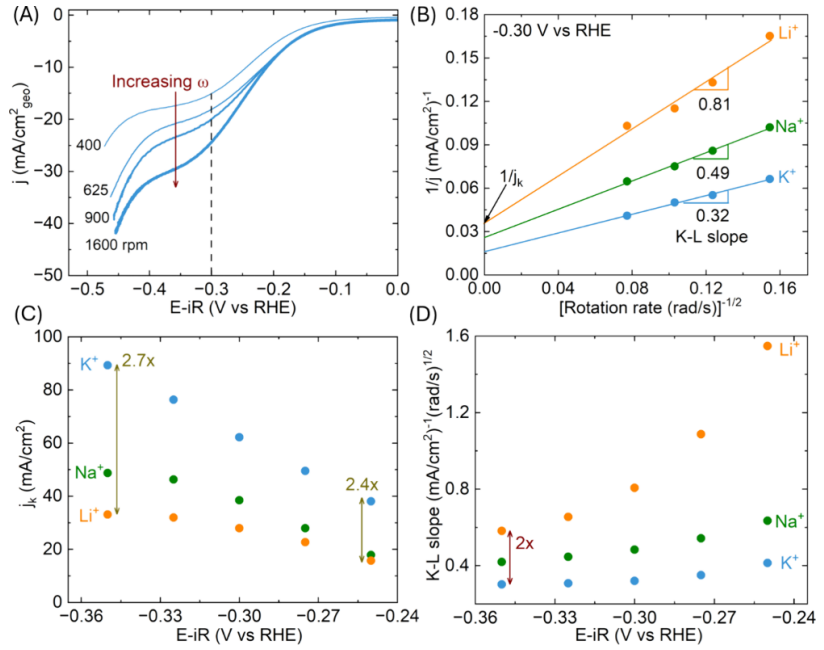

Figure 3. Rotation rate dependence of NO3RR on Co with 5 mM MNO_3 in 0.138 M *M*OH. (A) Cathodic sweep of CVs at noted rotation rate in rpm for $M = K^+$. (B) Example of Koutecky–Levich analysis at –0.3 V vs RHE, with noted K–L slopes and further fitting parameters in Table S1. (C) Kinetic current density j_k from the inverse of the y-intercept of panel (B); and (D) Koutecky–Levich (K-L) slope for noted cation in a supporting electrolyte of 0.138 M *M*OH (where $M = Li^+$, Na^+, K^+). Rotation rate-dependent data for Li^+ and Na^+ can be found in Figure S3.

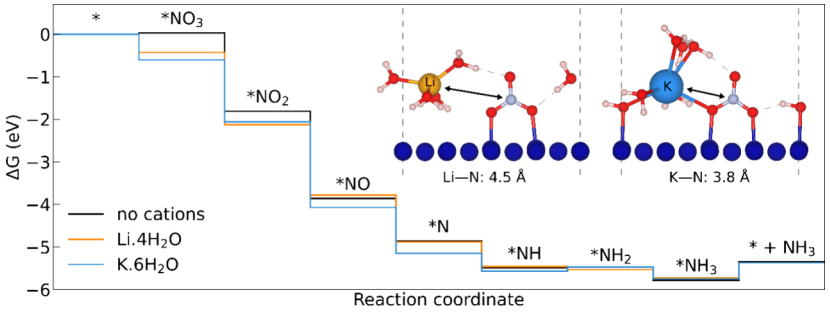

Figure 4. DFT-calculated free energy diagram for $*NO_x$ species adsorbed on the Co surface in the presence of solvated Li^+ and K^+ cations.

can also lead to specific interaction of K^+ with an oxygen of bound $*NO_3$ in addition to hydrogen bonding from its solvating waters, strengthening nitrate adsorption (Tables S4–S6). In contrast, strongly solvated Li^+ remains further away and interacts only via hydrogen bonding.

3.3. Cation-Dependent Effective Diffusion Coefficients

Returning to our experimental findings, the slopes from Koutecky–Levich (K–L) analysis are notably higher for Li^+ (Figure 3d), consistent with a ∼2x smaller D_{eff} than for K^+ (Table S2). Indeed, recent calculations predict a smaller diffusion coefficient for NO_3^- with a Li^+ cation, but only by ∼10%.[25] The smaller diffusion coefficients measured here via the rotation-dependent rate of anion reduction in comparison to bulk self-diffusion coefficients[25,48] could point to slower diffusion through the electrical double layer (EDL), particularly with Na^+ and Li^+. A similar reduction in diffusion from K–L analysis of Cl^- oxidation was attributed to a cation-dependent penetration of the EDL, modeled with an effective diffusion coefficient in the EDL three orders of magnitude smaller than in the bulk. We note that the magnitude of the cation dependence in D_{eff} found here was not observed for the outer sphere reduction of anions[38] or the inner sphere reduction of uncharged species (Figure S1),[3] but a similar magnitude has been observed for the inner sphere oxidation of anions, where the smaller value for Li^+ is attributed to its structure-making properties.[49] The flux of NO_3^- to the surface was also calculated by Murphy and Fong to be further suppressed for Li^+ from differences in transference number in the absence of a supporting electrolyte,[25] however, which may also play a more minor role here. It was surprising, however, to see that the experimental K–L slope measured here varied with applied potential for all cations (Figure 3d). Eq 3 suggests that a larger K–L slope at less cathodic potentials arises from either smaller *C** (unphysical; we note that the K–L slope decreases with concentration, Table S3) or a smaller diffusion coefficient. While back migration at the EDL could impact observed diffusion rates (via electrostatic repulsion in the opposite direction), the net effective diffusion coefficient would be expected to increase at less

https://doi.org/10.1021/acscatal.6c02764
ACS Catal. XXXX, XXX, XXX–XXX

cathodic potentials (where the surface charge is less negative), the opposite of the observed findings.

Instead, we reconsider the assumptions implicit in the analysis of areal current density. This geometric disk area (as opposed to one considering surface roughness) is appropriate in considering diffusion of NO_3^- through the stagnant layer to the surface. However, the catalyst could undergo dynamic changes in the availability of active sites with applied potential (e.g., resulting from redox events). If a reduction in active site density is appreciable relative to the exposed area of the disk, this would be observed as an increase in the K–L slope (eq 3, i.e., inversely proportional to the diffusion limited current). Thus, one possible explanation of the voltage-dependent K–L slope is that the cobalt surface changes over the course of the measurement. Such a change may also depend on the nature of the cation, and the density of active sites impacts interpretation of calculated kinetic rates.

3.4. Interrogating Surface Oxidation Processes

To investigate the ability of cobalt to undergo redox events at the electrochemical potentials considered, we performed *operando* XAS at the cobalt K-edge on Co nanoparticles for greater surface sensitivity (further details are in the ESI). Changes in the X-ray absorption near-edge structure (XANES) aid in quantifying the oxidation state, and changes in the extended X-ray absorption fine structure (EXAFS) inform on the local coordination environment. At reducing potentials of −0.37 V vs RHE where NO3RR is often measured, cobalt is dominated by the metallic state in both Li^+- and K^+-containing electrolytes (Figure 5b). However, at +0.3 V vs RHE, selected as a fixed value near the observed open circuit potential (OCP, Figure S10), extensive oxidation in ∼25 nm particles is observed (Figure 5b).

The changes in the local coordination environment and speciation of Co at different applied potentials are evident from the differences in the R-space peaks in the magnitude of the Fourier-transformed (FT) EXAFS (Figures 5d and S11). Based on linear combination fitting (LCF) analysis of the XANES spectra, we find that the Co is oxidized to greater extents in K^+-containing electrolyte compared to Li^+ at +0.3 V vs RHE, and the local coordination environment contains a greater amount of CoOOH, whereas Li^+ has a greater contribution from $Co(OH)_2$ (details of LCF are provided in the ESI, Figure S12 and Table S7). Although these oxides are eventually reduced under cathodic potentials (Figure S13), this occurs over many minutes and suggests that oxidized sites at the surface and/or subsurface may indeed be present during NO3RR measurements, and to different extents, dependent on the electrolyte cation identity.

3.5. The Role of Oxide on NO3RR and NO2RR Rates

To interrogate the role this oxidized phase may have on NO3RR kinetics and site availability, we performed an initial CV on an HCl-treated cobalt disk (minimizing oxidation) and followed this by a hold at +0.3 V vs RHE (∼OCP), and another CV to NO3RR conditions. In K^+-containing electrolytes, the kinetic- and mass transfer-limited cathodic currents are *reduced* slightly following the +0.3 V vs RHE hold, whereas in Li^+-containing electrolytes, both regions of the CV are notably *promoted* (Figure 5a).

The ability of NO_3^- to oxidize a metallic Co surface is anticipated, given the difference in formal potentials for NO_3^-/NO_2^- and Co/Co(II) redox.[33] Indeed, spontaneous redox has been

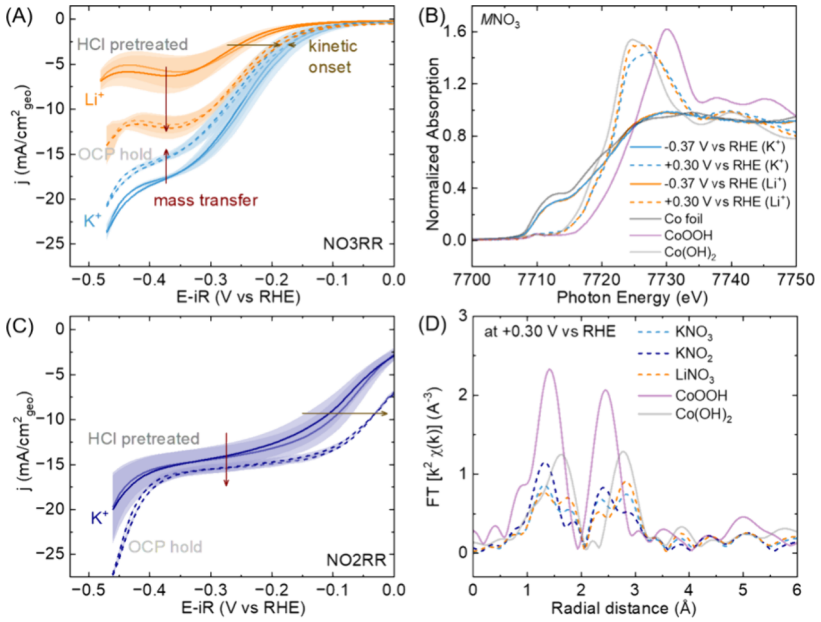

Figure 5. (A and C) Cobalt RDE at 400 rpm for (A) 5mM MNO_3 in 0.138 M MOH ($M = K^+$, Li^+), (C) 5 mM KNO_2 in 0.138 M KOH; solid line: HCl-cleaned Co disk, dashed line: after CA hold at OCP (0.3 V vs RHE) for 3 min 10 s. The average current measured during the forward and reverse sweep of a 10 mV/s CV is presented, along with the standard deviation as a shaded bar from three independent measurements. (B and D) Co K-edge XANES collected under *operando* conditions during the NO3RR process on Co nanoparticles. The steady state spectra at each potential are shown here; further details are in the ESI. (B) XANES at −0.37 V vs RHE (solid) and OCP (+0.3 V vs RHE, dashed) in K^+-(blue) and Li^+-(orange) containing electrolyte. (D) Magnitude of the Fourier transforms (FTs) of k^2-weighted EXAFS spectra in different electrolytes. Dashed lines represent corresponding EXAFS data at +0.3 V vs RHE, and the solid lines are from ex situ reference compounds.

https://doi.org/10.1021/acscatal.6c02764
ACS Catal. XXXX, XXX, XXX–XXX

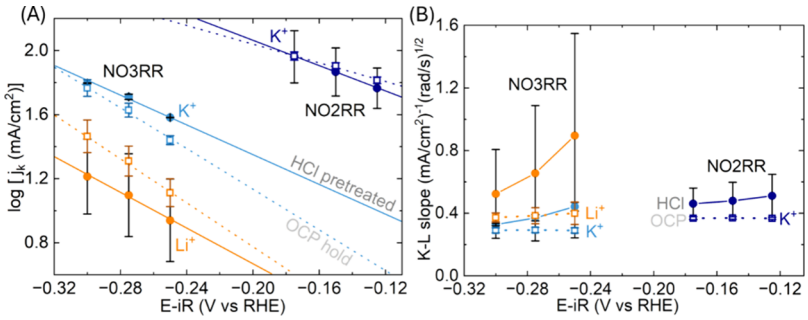

Figure 6. K–L analysis of Co disk with HCl pretreatment (solid circles and lines) and following an OCP hold (open squares and dashed lines) for 5 mM MNO_3 (or KNO_2) in 0.138 M MOH, where $M = K^+$ (blue) or Li^+ (orange). A) Log of the average kinetic current density j_k and B) average K–L slope.

suggested as the mechanism of NO_3^- adsorption during NO3RR on Co.[17,33] However, the involvement of a facile chemical step is surprising given the fact that the onset of sustained kinetic current from NO3RR is more than 100 mV more cathodic than for NO2RR (Figure 5c), and the kinetic current for NO2RR is approximately an order of magnitude greater (Figure S14). This observation suggests that the potential determining step for NO3RR is prior to the formation of NO_2* on the surface. Of further surprise is the fact that the NO2RR with K^+ is promoted by a potential hold at ∼OCP (+0.3 V vs RHE), where XAS again indicates extensive oxidation of cobalt (Figure S15). This promotion of NO2RR following a hold at +0.3 V vs RHE is also observed in Na^+-containing electrolyte (Figure S16).

We next disentangle kinetic- and mass transport-limited currents via Koutecky–Levich analysis for Co following a hold at ∼OCP (+0.3 V vs RHE) where spontaneous redox occurs. Indeed, NO3RR kinetic current is enhanced for Li^+-containing electrolytes, but suppressed in K^+ electrolytes (Figure 6a). However, the kinetic current in K^+ is still ∼2x larger. In contrast to the (initially) metallic surface (solid markers and lines), the Koutecky–Levich slope (reflecting mass transport limitations controlled by the thickness of the stagnant layer) is potential independent following OCP pretreatment (Figure 6b, open markers and dashed lines), suggesting that the (partially) oxidized surface is kinetically stabilized. The K–L slope (eq 3) remains higher in Li^+- versus K^+-containing electrolyte, consistent with a smaller C* (unphysical), smaller effective surface area, and/or a smaller effective diffusion coefficient.

As discussed above, the smaller solvated radius of K^+ is consistent with a higher electric field strength than with Li^+,[50] and the ∼2x higher D_{eff} we measure with K^+ vs Li^+ (Table S2) may arise from a combination of a slightly higher diffusion coefficient of NO_3^- combined with a lower transference number for electrolytes with K^+.[25] However, the local field strength[51] and driving force for anion adsorption can both be influenced by the surface charge, dependent on the extent of (dynamic) oxidation. The potential of zero charge is generally lower for cobalt oxides than cobalt metal in alkaline media,[52,53] suggesting that a less negative surface charge of oxidized surfaces could indeed benefit mass transport of nitrate to the surface. This draws similarities to the electroreduction of the anion peroxodisulfate, suppressed when the surface is negatively charged.[54] The greater extent of oxidation observed by XAS in K^+-containing electrolyte may then also contribute to the higher mass transport-limited currents in comparison to Li^+-containing electrolytes via an electrostatic promotion of adsorption at nearby reduced metal centers. We note that the NO3RR Tafel slope is reduced following an OCP hold (∼125 mV/decade vs ∼195 mV/decade) regardless of cation identity (Table S8), also found for HER (Figure S9).

3.6. Implications on NO3RR and NO2RR Mechanistic Understanding

The trends in both kinetic- and mass transport-limited currents with persistent (hydr)oxides in NO3RR and NO2RR give additional mechanistic insight into likely rate-determining steps. We highlight that (1) NO3RR is favored with intentional oxidation for Li^+ but not K^+, and (2) NO2RR is favored with intentional oxidation for K^+ but not NO3RR. One possible explanation for this finding is that nitrate (and nitrite) adsorption at more cathodic potentials is promoted by the coexistence of metallic and oxidized Co sites, making the surface charge less negative/stabilizing water deprotonation. Here, oxidized sites promote nitrate and nitrite adsorption via modulation of surface charge but ultimately reduce the number of active sites involved in the reaction, whereas in situ-generated reduced active metallic Co sites promote site utilization for NO3RR. Optimizing these two effects is crucial to observe higher NO3RR rates. For NO3RR in K^+, the rate-determining step may be the regeneration of active (metallic) sites for NO_3^- adsorption, whereas Li^+ may promote dynamic surface reduction to greater extents, meriting further study.

4. CONCLUSIONS

We isolate the impact of cation identity on two important aspects of NO3RR—kinetics and mass transfer—which have been consistently convoluted in reports of NO3RR "activity" to date. Surprisingly, we find that the mass transfer-limited current is ∼2-fold greater for K^+- vs Li^+-containing electrolytes, a difference that does not persist in considering outer-sphere electron transfer reactions or for neutral inner-sphere reactants. Accounting for this, however, the kinetic current is still 2–3x greater in K^+- vs Li^+-containing electrolytes. Calculations show that cations can stabilize the adsorption of NO_3^-, and, to greater extents, for K^+. A higher electric field strength for K^+ can also explain the higher rates of reduction for polar rate-determining intermediates in the NO3RR, and a similarly

https://doi.org/10.1021/acscatal.6c02764
ACS Catal. XXXX, XXX, XXX–XXX

higher rate is observed for K^+ vs Na^+ in NO2RR. Inseparable from this picture of the electrical double layer, however, is the ability of NO_3^- to oxidize Co during adsorption occurring more extensively with the K^+-containing electrolyte. This oxidation is expected to promote NO_3^- transport to and adsorption on the surface from the electrostatic perspective, but fundamentally reduces the number of metallic active sites available for NO_3^- adsorption. These findings indicate that cation identity plays an additional unique role for NO3RR in alkaline media by controlling the rates of reducing surface oxides in a dynamic process enabling adsorption of the NO_3^- anion at such reducing potentials, otherwise unexpected from an electrostatics perspective.

■ ASSOCIATED CONTENT

Supporting Information

The Supporting Information is available free of charge at https://pubs.acs.org/doi/10.1021/acscatal.6c02764.

Experimental methods, electrochemical measurements, conversion measurement and product quantification, analytical model, density functional theory, operando XAS measurements and additional results; electrochemical data and fitting parameters (PDF)

■ AUTHOR INFORMATION

Corresponding Author

Kelsey A. Stoerzinger – *Department of Chemical Engineering and Material Science, University of Minnesota, Minneapolis, Minnesota 55455, United States; School of Chemical, Biological, and Environmental Engineering, Oregon State University, Corvallis, Oregon 97331, United States;* orcid.org/0000-0002-3431-8290; Email: zinger@umn.edu

Authors

Rajkumar Jana – *Department of Chemical Engineering and Material Science, University of Minnesota, Minneapolis, Minnesota 55455, United States; School of Chemical, Biological, and Environmental Engineering, Oregon State University, Corvallis, Oregon 97331, United States;* orcid.org/0000-0001-7463-6202

O. Quinn Carvalho – *School of Chemical, Biological, and Environmental Engineering, Oregon State University, Corvallis, Oregon 97331, United States*; Present Address: Materials Chemical and Computational Science Directorate, National Renewable Energy Laboratory, Golden, Colorado 80401, United States.; orcid.org/0000-0003-4420-5203

Ruth Bello – *Department of Chemical Engineering and Material Science, University of Minnesota, Minneapolis, Minnesota 55455, United States*

Payal Chaudhary – *Department of Chemical and Biomolecular Engineering, University of Nebraska-Lincoln, Lincoln, Nebraska 68588, United States;* orcid.org/0000-0002-8863-5646

Jiyun Hong – *Stanford Synchrotron Radiation Lightsource, SLAC National Accelerator Laboratory, Menlo Park, California 94025, United states;* orcid.org/0000-0002-3631-0559

Adam S. Hoffman – *Stanford Synchrotron Radiation Lightsource, SLAC National Accelerator Laboratory, Menlo Park, California 94025, United states*

Simon R. Bare – *Stanford Synchrotron Radiation Lightsource, SLAC National Accelerator Laboratory, Menlo Park, California 94025, United states;* orcid.org/0000-0002-4932-0342

Ankur Gupta – *Department of Chemical and Biological Engineering, University of Colorado Boulder, Boulder, Colorado 80303, United states;* orcid.org/0000-0003-3474-9522

Vitaly Alexandrov – *Department of Chemical and Biomolecular Engineering, University of Nebraska-Lincoln, Lincoln, Nebraska 68588, United States;* orcid.org/0000-0003-2063-6914

Complete contact information is available at: https://pubs.acs.org/doi/10.1021/acscatal.6c02764

Notes

The authors declare the following competing financial interest(s): K.A.S. is an associate editor of ACS Catalysis, but was not involved in the handling of this manuscript.

■ ACKNOWLEDGMENTS

This material is based upon work supported by the U.S. Department of Energy, Office of Science, Basic Energy Sciences, Chemical Sciences, Geosciences, and Biosciences Division, Catalysis program under Award numbers DE-SC0022970 and DE-SC0024865. A.G. acknowledges the NSF award #2238412 for support of computational modeling. V.A. acknowledges the National Science Foundation support through the NSF CAREER award (CBET-1941204) for support of DFT calculations. The use of the Stanford Synchrotron Radiation Lightsource, SLAC National Accelerator Laboratory, is supported by the U.S. Department of Energy, Office of Science, Office of Basic Energy Sciences under Contract No. DE-AC02-76SF00515. Support from Co-ACCESS, part of the SUNCAT Center for Interface Science and Catalysis, was provided by the DOE BES, Chemical Sciences, Geosciences, and Biosciences Division.

■ REFERENCES

(1) Sebastián-Pascual, P.; Shao-Horn, Y.; Escudero-Escribano, M. Toward understanding the role of the electric double layer structure and electrolyte effects on well-defined interfaces for electrocatalysis. *Curr. Opin. Electrochem.* **2022**, *32*, No. 100918.

(2) Brown, M. A.; Abbas, Z.; Kleibert, A.; Green, R. G.; Goel, A.; May, S.; Squires, T. M. J. P. R. X. Determination of surface potential and electrical double-layer structure at the aqueous electrolyte-nanoparticle interface. *J. Phys. Rev. X* **2016**, *6* (1), No. 011007.

(3) Bender, J. T.; Sanspeur, R. Y.; Valles, A. E.; Uvodich, A. K.; Milliron, D. J.; Kitchin, J. R.; Resasco, J. The potential of zero total charge predicts cation effects for the oxygen reduction reaction. *ACS Energy Lett.* **2024**, *9* (9), 4724–4733.

(4) Resasco, J.; Chen, L. D.; Clark, E.; Tsai, C.; Hahn, C.; Jaramillo, T. F.; Chan, K.; Bell, A. T. Promoter effects of alkali metal cations on the electrochemical reduction of carbon dioxide. *J. Am. Chem. Soc.* **2017**, *139* (32), 11277–11287.

(5) Ringe, S.; Clark, E. L.; Resasco, J.; Walton, A.; Seger, B.; Bell, A. T.; Chan, K.Understanding cation effects in electrochemical CO_2 reduction. *Energy Environ. Sci.* **2019**, *12* (10), 3001–3014.

(6) Sargeant, E.; Rodriguez, P.; Calle-Vallejo, F.Cation Effects on the Adsorbed Intermediates of CO_2 Electroreduction Are Systematic and Predictable. *ACS Catal.* **2024**, *14* (11), 8814–8822.
(7) Singh, M. R.; Kwon, Y.; Lum, Y.; Ager, J. W., III; Bell, A. T.Hydrolysis of Electrolyte Cations Enhances the Electrochemical Reduction of CO_2 over Ag and Cu. *J. Am. Chem. Soc.* **2016**, *138* (39), 13006–13012.
(8) Goyal, A.; Louisia, S.; Moerland, P.; Koper, M. T. M. Cooperative Effect of Cations and Catalyst Structure in Tuning Alkaline Hydrogen Evolution on Pt Electrodes. *J. Am. Chem. Soc.* **2024**, *146* (11), 7305–7312.
(9) Huang, B.; Rao, R. R.; You, S.; Hpone Myint, K.; Song, Y.; Wang, Y.; Ding, W.; Giordano, L.; Zhang, Y.; Wang, T.; Muy, S.; Katayama, Y.; Grossman, J. C.; Willard, A. P.; Xu, K.; Jiang, Y.; Shao-Horn, Y. Cation- and pH-Dependent Hydrogen Evolution and Oxidation Reaction Kinetics. *JACS Au* **2021**, *1* (10), 1674–1687.
(10) Shah, A. H.; Zhang, Z.; Huang, Z.; Wang, S.; Zhong, G.; Wan, C.; Alexandrova, A. N.; Huang, Y.; Duan, X. The role of alkali metal cations and platinum-surface hydroxyl in the alkaline hydrogen evolution reaction. *Nat. Catal.* **2022**, *5* (10), 923–933.
(11) Monteiro, M. C. O.; Goyal, A.; Moerland, P.; Koper, M. T. M. Understanding Cation Trends for Hydrogen Evolution on Platinum and Gold Electrodes in Alkaline Media. *ACS Catal.* **2021**, *11* (23), 14328–14335.
(12) Wu, Q.; Xu, Z. J. Mechanistic Insights into Cation Effects in Electrolytes for Electrocatalysis. *Angew. Chem., Int. Ed.* **2025**, *64* (28), No. e202505022.
(13) Xu, A.; Govindarajan, N.; Kastlunger, G.; Vijay, S.; Chan, K.Theories for Electrolyte Effects in CO_2 Electroreduction. *Acc. Chem. Res.* **2022**, *55* (4), 495–503.
(14) Xu, P.; Wang, R.; Zhang, H.; Carnevale, V.; Borguet, E.; Suntivich, J. Cation Modifies Interfacial Water Structures on Platinum during Alkaline Hydrogen Electrocatalysis. *J. Am. Chem. Soc.* **2024**, *146* (4), 2426–2434.
(15) Bender, J. T.; Petersen, A. S.; Østergaard, F. C.; Wood, M. A.; Heffernan, S. M. J.; Milliron, D. J.; Rossmeisl, J.; Resasco, J. Understanding Cation Effects on the Hydrogen Evolution Reaction. *ACS Energy Lett.* **2023**, *8* (1), 657–665.
(16) Qian, S.-J.; Cao, H.; Lv, X.-M.; Li, J.; Wang, Y.-G. Elucidating the Activity of Electrochemical Nitrate Reduction: High-Valent Anionic Intermediates as Kinetic Gatekeepers. *J. Am. Chem. Soc.* **2025**, *147* (24), 21032–21040.
(17) Zhang, L.; Liu, Y.; Li, L.; Wu, T.; Wu, Q.; Seow, J. Z. Y.; Lin, X.; Sun, S.; Tannesia, L.; Tang, K.; Shao, D.; Xi, S.; Guo, X.; Xu, Z. J. High-efficiency ammonia electrosynthesis from nitrate on ruthenium-induced trivalent cobalt sites. *Energy Environ. Sci.* **2025**, *18* (11), 5622–5631.
(18) Liao, W.; Wang, J.; Tan, Y.; Zi, X.; Liu, C.; Wang, Q.; Zhu, L.; Kao, C.-W.; Chan, T.-S.; Li, H.; Zhang, Y.; Liu, K.; Cai, C.; Fu, J.; Xi, B.; Cortés, E.; Chai, L.; Liu, M. Near-Unity Nitrate to Ammonia conversion via reactant enrichment at the solid-liquid interface. *Nat. Commun.* **2025**, *16* (1), 5715.
(19) Souza-Garcia, J.; Ticianelli, E. A.; Climent, V.; Feliu, J. Nitrate reduction on Pt single crystals with Pd multilayer. *Electrochim. Acta* **2009**, *54* (7), 2094–2101.
(20) Kelly, S. R.; Heenen, H. H.; Govindarajan, N.; Chan, K.; Nørskov, J. K. OH binding energy as a universal descriptor of the potential of zero charge on transition metal surfaces. *J. Phys. Chem. C* **2022**, *126* (12), 5521–5528.
(21) Slesinska, S.; Galek, P.; Menzel, J.; Donne, S. W.; Fic, K.; Płatek-Mielczarek, A. Fundamentals and Implication of Point of Zero Charge (PZC) Determination for Activated Carbons in Aqueous Electrolytes. *Adv. Sci.* **2024**, *11* (48), No. 2409162.
(22) Hussain, G.; Pérez-Martínez, L.; Le, J.-B.; Papasizza, M.; Cabello, G.; Cheng, J.; Cuesta, A.How cations determine the interfacial potential profile: Relevance for the CO_2 reduction reaction. *Electrochim. Acta* **2019**, *327*, No. 135055.
(23) Shin, S.-J.; Kim, D. H.; Bae, G.; Ringe, S.; Choi, H.; Lim, H.-K.; Choi, C. H.; Kim, H. On the importance of the electric double layer structure in aqueous electrocatalysis. *Nat. Commun.* **2022**, *13* (1), 174.
(24) Guo, J.; Brimley, P.; Liu, M. J.; Corson, E. R.; Muñoz, C.; Smith, W. A.; Tarpeh, W. A. Mass transport modifies the interfacial electrolyte to influence electrochemical nitrate reduction. *ACS Sustain. Chem. Eng.* **2023**, *11* (20), 7882–7893.
(25) Murphy, M. A.; Fong, K. D. Beyond Interfacial Structure: Ion Transport Mediates Cation Effects in Electrochemical Nitrate Reduction. *ACS Electrochem.* **2026**, *2*, 983.
(26) Katsounaros, I.; Kyriacou, G. Influence of the concentration and the nature of the supporting electrolyte on the electrochemical reduction of nitrate on tin cathode. *Electrochim. Acta* **2007**, *52* (23), 6412–6420.
(27) Wen, W.; Fang, S.; Zhou, Y.; Zhao, Y.; Li, P.; Yu, X. Y. Modulating the electrolyte microenvironment in electrical double layer for boosting electrocatalytic nitrate reduction to ammonia. *Angew. Chem., Int. Ed.* **2024**, *63* (32), No. e202408382.
(28) Zhou, J.; Liu, F.; Xu, Z.; Yin, J.-A.; Guo, L.; Hao, F.; Wang, Y.; Xiong, Y.; Zhou, X.; Wang, C.; Ma, Y.; Meng, X.; Lu, P.; Yin, J.; Zhang, A.; Wang, J.; Ye, C.; Li, Q.; Ling, C.; Chen, H.-C.; Chen, H. M.; Zhu, Y.; Lu, J.; Fan, Z. Modulating the Nitrate Reduction Pathway on Unconventional Phase Ultrathin Nanoalloys for Selective Ammonia Electrosynthesis. *J. Am. Chem. Soc.* **2025**, *147* (26), 23226–23238.
(29) Ahmadi, M.; Nazemi, M. Understanding potential losses and pH distribution in the electrochemical nitrate reduction reaction to ammonia. *Ind. Eng. Chem. Res.* **2024**, *63* (21), 9315–9328.
(30) Pathak, D. K.; Jana, R.; Bello, R.; White, K.; Stoerzinger, K. A. Robust catalyst assessment for the electrocatalytic nitrate reduction reaction. *Commun. Chem.* **2025**, *8* (1), 302.
(32) Tao, J.; Yang, W.; Pei, F.; Cui, X. Co-based tandem catalysts for electrocatalytic nitrate reduction: mechanisms and challenges. *Chem. Commun.* **2025**, *61* (93), 18236–18246.
(33) Han, S.; Li, H.; Li, T.; Chen, F.; Yang, R.; Yu, Y.; Zhang, B. Ultralow overpotential nitrate reduction to ammonia via a three-step relay mechanism. *Nat. Catal.* **2023**, *6* (5), 402–414.
(34) Shim, M.; Ko, J.; Kim, Y.; Jung, Y.; Byon, H. R. Oxygen Poisoning of Copper Surfaces in the Presence of Cesium Ions during Electrochemical Nitrate Reduction to Ammonia. *ACS Catal.* **2025**, *15* (13), 11695–11704.
(35) Carvalho, O. Q.; Marks, R.; Nguyen, H. K. K.; Vitale-Sullivan, M. E.; Martinez, S. C.; Arnadottir, L.; Stoerzinger, K. A. Role of Electronic Structure on Nitrate Reduction to Ammonium: A Periodic Journey. *J. Am. Chem. Soc.* **2022**, *144* (32), 14809–14818.
(36) Yang, K.; Han, S.-H.; Cheng, C.; Guo, C.; Li, T.; Yu, Y. Unveiling the Reaction Mechanism of Nitrate Reduction to Ammonia Over Cobalt-Based Electrocatalysts. *J. Am. Chem. Soc.* **2024**, *146* (19), 12976–12983.
(37) Meng, X.; Tan, X.; Ma, Y.; Obisanya, A. A.; Wang, J.; Xiao, Z.; Wang, D. Recent Progress in Cobalt-Based Electrocatalysts for Efficient Electrochemical Nitrate Reduction Reaction. *Adv. Funct. Mater.* **2025**, *35* (14), No. 2418492.
(38) Huang, B.; Myint, K. H.; Wang, Y.; Zhang, Y.; Rao, R. R.; Sun, J.; Muy, S.; Katayama, Y.; Corchado Garcia, J.; Fraggedakis, D. Cation-dependent interfacial structures and kinetics for outer-sphere electron-transfer reactions. *J. Phys. Chem. C* **2021**, *125* (8), 4397–4411.
(39) Rhine, E. D.; Mulvaney, R. L.; Pratt, E. J.; Sims, G. K. Improving the Berthelot Reaction for Determining Ammonium in Soil Extracts and Water. *Soil Sci. Soc. Am. J.* **1998**, *62* (2), 473–480.
(40) Ostervold, L.; Hoffman, A. S.; Thompson, D.; Bare, S. R.; Clark, E. L. A Versatile Electrochemical Cell for Operando XAS. *ChemCatChem* **2024**, *16* (15), No. e202400072.
(41) Kresse, G.; Furthmüller, J. Efficient iteratives for ab initio total-energy calculations using a plane-wave basis set. *Phys. Rev. B* **1996**, *54* (16), 11169–11186.

https://doi.org/10.1021/acscatal.6c02764
ACS Catal. XXXX, XXX, XXX–XXX

(42) Kresse, G.; Furthmüller, J. Efficiency of ab-initio total energy calculations for metals and semiconductors using a plane-wave basis set. *Comput. Mater. Sci.* **1996**, *6* (1), 15–50.
(43) Kresse, G.; Joubert, D. From ultrasoft pseudopotentials to the projector augmented-wave method. *Phys. Rev. B* **1999**, *59* (3), 1758–1775.
(44) Perdew, J. P.; Burke, K.; Ernzerhof, M. Generalized Gradient Approximation Made Simple. *Phys. Rev. Lett.* **1996**, *77* (18), 3865–3868.
(45) Grimme, S.; Antony, J.; Ehrlich, S.; Krieg, H. A consistent and accurate ab initio parametrization of density functional dispersion correction (DFT-D) for the 94 elements H-Pu. *J. Chem. Phys.* **2010**, *132* (15), 154104.
(46) Calle-Vallejo, F.; Huang, M.; Henry, J. B.; Koper, M. T. M.; Bandarenka, A. S. Theoretical design and experimental implementation of Ag/Au electrodes for the electrochemical reduction of nitrate. *Phys. Chem. Chem. Phys.* **2013**, *15* (9), 3196–3202.
(47) Bard, A. J.; Faulkner, L. R.; White, H. S. *Electrochemical methods: fundamentals and applications*; John Wiley and Sons, **2022**.
(48) Hashitani, T.; Tanaka, K. Measurements of self-diffusion coefficients of the nitrate ion in aqueous solutions of potassium nitrate and calcium nitrate. *J. Chem. Soc., Faraday Trans. 1* **1983**, *79* (8), 1765–1768.
(49) Lim, T.; Ooka, H.; Yu, Y.; Murakami, T.; Wada, S.; Nakamura, R. Hydration entropy of cations regulates chloride ion diffusion during electrochemical chlorine evolution. *Nat. Chem.* **2026**, *18* (3), 552–560.
(50) Bohra, D.; Chaudhry, J. H.; Burdyny, T.; Pidko, E. A.; Smith, W. A.Modeling the electrical double layer to understand the reaction environment in a CO_2 electrocatalytic system. *Energy Environ. Sci.* **2019**, *12* (11), 3380–3389.
(51) Mohandas, N.; Bawari, S.; Shibuya, J. J. T.; Ghosh, S.; Mondal, J.; Narayanan, T. N.; Cuesta, A. Understanding electrochemical interfaces through comparing experimental and computational charge density–potential curves. *Chem. Sci.* **2024**, *15* (18), 6643–6660.
(52) Muhyuddin, M.; Pianta, N.; Trindell, J. A.; Ruffo, R.; Santoro, C.; Koper, M. T. M. Cation Effects on the Hydrogen Evolution Reaction by Catalysts Based on Cobalt Complexes in Alkaline Electrolytes. *Electrochim. Acta* **2025**, *535*, No. 146684.
(53) McCafferty, E. Relationship between the isoelectric point (pHpzc) and the potential of zero charge (Epzc) for passive metals. *Electrochim. Acta* **2010**, *55* (5), 1630–1637.
(54) Martínez-Hincapié, R.; Climent, V.; Feliu, J. M. Peroxodisulfate reduction as a probe to interfacial charge. *Electrochem. Commun.* **2018**, *88*, 43–46.

https://doi.org/10.1021/acscatal.6c02764
ACS Catal. XXXX, XXX, XXX–XXX